

In-plane electronic confinement in superconducting LaAlO₃/SrTiO₃ nanostructures

D. Stornaiuolo,^{1, a)} S. Gariglio,¹ N.J.G. Couto,^{1, 2} A. Fête,¹ A. D. Caviglia,^{1, b)} G. Seyfarth,^{1, c)} D. Jaccard,¹ A.F. Morpurgo,^{1, 2} and J.-M. Triscone¹

¹⁾*DPMC - University of Geneva, 24 quai Ernest-Ansermet, CH-1211 Geneva, Switzerland*

²⁾*GAP - University of Geneva, 24 quai Ernest-Ansermet, CH-1211 Geneva, Switzerland*

(Dated: 24 January 2018)

We describe the transport properties of mesoscopic devices based on the two dimensional electron gas (2DEG) present at the LaAlO₃/SrTiO₃ interface. Bridges with lateral dimensions down to 500 nm were realized using electron beam lithography. Their detailed characterization shows that processing and confinement do not alter the transport parameters of the 2DEG. The devices exhibit superconducting behavior tunable by electric field effect. In the normal state, we measured universal conductance fluctuations, signature of phase-coherent transport in small structures. The achievement of reliable lateral confinement of the 2DEG opens the way to the realization of quantum electronic devices at the LaAlO₃/SrTiO₃ interface.

^{a)}Electronic mail: daniela.stornaiuolo@unige.ch

^{b)}now at Max-Planck Research Group for Structural Dynamics-Center for Free Electron Laser Science, University of Hamburg, Notkestrasse 85, 22607 Hamburg, Germany

^{c)}now at LNCMI-G, CNRS, 25 rue des Martyrs, 38042 GRENOBLE cedex 9, France

Since its discovery,¹ the two dimensional electron gas present at the interface between the two insulators LaAlO₃ and SrTiO₃ (LAO/STO) has been the subject of intense study. This large effort has brought to light a variety of physical phenomena exhibited at this interface, making it one of the most fascinating systems in the field of oxide electronics.^{2,3} The 2DEG undergoes a superconducting transition with a maximum critical temperature of ≈ 300 mK,⁴ which can be gate tuned, allowing the superconducting state to be switched on and off.^{5,6} Magnetotransport measurements have shown that, concomitantly with the superconducting state, a large Rashba spin-orbit interaction sets in.^{7,8} The out-of-plane confinement of the electron gas, estimated to be on the scale of a few nanometres,^{9,10} gives rise to two-dimensional electronic states, as recently observed via angle-dependent Shubnikov-de Haas oscillations.^{11,12}

The physical parameters obtained from the electronic band structure and the transport analyses are radically different from those of the 2DEGs found in classical semiconductor heterostructures, making this oxide interface particularly interesting for the study of mesoscopic effects.^{2,13} For instance, the Fermi and the Rashba spin-splitting energies are comparable (~ 10 meV). Additionally, in the presence of a magnetic field, the large effective mass makes the Zeeman energy larger than the Landau level splitting, a situation markedly different from the one found in III - V heterostructures. The breaking of inversion symmetry could also be at the origin of a mixing of a singlet and triplet superconducting pairing state, which can be investigated using tunnel junctions in spectroscopy experiments.^{14,15} The realization of nanostructures is fundamental in order to explore these unconventional regimes. Two nanofabrication techniques have been applied up to now to this system. In the first one, the voltage-biased metallic tip of an atomic force microscope is scanned over the surface of a 3 unit cell (u.c.) thick LAO film, locally inducing a conducting channel at the interface. Metallic lines as narrow as a few nanometres have been created and measured.¹⁶⁻¹⁸ The second approach relies on the use of electron beam lithography,¹⁹ which allows greater flexibility for the realization of devices with complex geometries and longer lifetime. However, the evolution of the transport parameters with the bridge size and the possible effects of the fabrication process on the 2DEG's normal and superconducting properties need to be fully addressed in order to exploit the full potential of LAO/STO for nano-electronics.

In this letter, we describe a systematic study of the transport properties of LAO/STO-based nanostructures realized by electron beam lithography. We show that the mobility

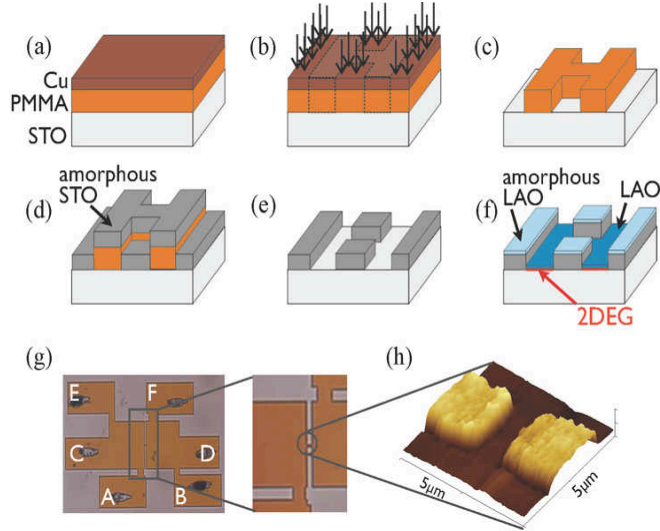


FIG. 1. (Color online) Sketch of the fabrication process: (a) deposition of PMMA and Cu layers, (b) e-beam exposure, (c) development of PMMA (after the Cu wet etch), (d) deposition of amorphous STO and (e) lift off, (f) deposition of the LAO film. In panel (g) an optical microscope image of one of the devices is shown before the amorphous STO lift-off procedure (full scale: $1.5 \text{ mm} \times 1.2 \text{ mm}$). Panel (h) shows an atomic force microscope image of the bridge area. Polycrystalline/amorphous LAO, grown on the amorphous STO, has a lighter color, while the epitaxial LAO has a darker one. The 2DEG is created only below the epitaxial LAO.

and carrier density of bridges with lateral dimensions down to 500 nm are unaffected by the fabrication process and are comparable with those of large area devices. At low temperature, these bridges exhibit superconducting behavior with a critical current that can be modulated using the field effect. For magnetic fields large enough to suppress superconductivity, magnetoresistance measurements display universal conductance fluctuations (UCF). As UCF stem from phase-coherent transport,^{5,7,20} their observation indicates that the devices fabricated with the technique described in this paper allow the mesoscopic transport regime to be accessed.

The steps for the fabrication of nanoscale bridges are illustrated in Figure 1. The process avoids an ion milling step, which could damage the STO crystal with, for instance, the creation of oxygen vacancies.²¹ A template with the desired pattern is realized on the substrates by depositing an amorphous STO layer before the epitaxial growth of the LAO thin film. To this purpose, we pattern a resist mask on the bare STO substrate (Figures 1(a), (b) and (c))

using an electron beam lithography procedure optimized for insulating materials. Specifically, prior to exposure, we cover the PMMA resist with a thin film of copper (7 nm, see Figure 1(a))²². This metallic film acts as a charge dispersion layer, reducing accumulation of surface charges on the STO insulating substrate. It has a minimal influence on the pattern resolution, while increases slightly the exposure dose required for PMMA.²³ After exposure, the copper layer is removed by wet etching using a solution of FeCl in water, then the PMMA is developed using a diluted methyl isobutyl ketone (MIBK) solution, revealing the pattern. After development, we deposit a thin layer (15 nm) of amorphous STO (Figure 1(d)), before removing the resist with a lift-off procedure. Thus we obtain a template substrate with the desired pattern made of an amorphous STO layer (Figure 1(e)).²⁴ Finally, an epitaxial 10 u.c.-thick LAO film is deposited using pulsed laser deposition (Figure 1(f)).²⁵ The film is grown at 800°C in 10^{-4} mbar of oxygen. The KrF excimer laser fluency is 0.6 J/cm² with a repetition rate of 1 Hz. Immediately after deposition, the sample is annealed in oxygen: we fill the deposition chamber with 200 mbar of oxygen and keep the sample temperature at 520°C for 1 hour. The sample is then slowly cooled down to room temperature in the same oxygen atmosphere.²⁶ The growth process is monitored *in situ* using reflection high energy electron diffraction (RHEED), which shows, for all the samples, a layer-by-layer growth mode. An atomic force microscope image of an 800 nm-wide and 2 μ m-long bridge realized with this technique is shown in Fig. 1(h).

We have fabricated several tens of bridges of different width, with good reproducibility of the transport parameters. Using the layout shown in Fig. 1(g), we are able to measure the properties of both the bridges and of the larger area adjoining each of them, using a four-point DC technique. We inject current through contacts C-D and measure the voltage drop between A and F to probe the bridges, and between B and F (or A and E) to probe the larger areas.

Figure 2(a) shows the metallic behavior of two devices, 500 nm (green line) and 800 nm (blue circles) wide, both 2 μ m-long, and of a large area of dimensions 300 μ m \times 300 μ m (orange squares). Figure 3(a) summarizes the sheet resistance R_S values measured at 1.5 K for devices of different size realized on the same chip and for the large areas adjoining each of them. Figure 2(b) displays the magnetoresistance $\Delta R/R(0) = (R(B) - R(0))/R(0)$ of the same devices, measured at 1.5 K. Fitting the quadratic behavior of the magnetoresistance with the relation^{27,28} $\Delta R/R(0) = (\mu B)^2$ (see for example the fit referring to the 500 nm

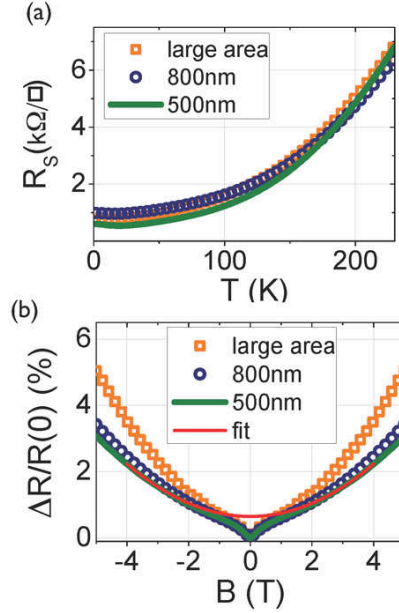


FIG. 2. (Color online) Transport properties of the mesoscopic devices. Panel (a) shows typical $R_S(T)$ curves of 500 nm (green line) and 800 nm (blue circles) bridges and of a large area ($300\mu m \times 300\mu m$) (orange squares). Panel (b) displays the relative magnetoresistance, measured at 1.5 K, for the same three devices. The magnetic field was applied perpendicular to the sample. The solid red line is an example of the quadratic fit used to extract the carrier mobilities.

bridge in Figure 2(b)), we estimate the mobility μ of the charge carriers for channels of different width as well as for the large areas. These data are plotted in Figure 3(b). From these measurements, we can also estimate the number of carriers in the bridge $n_{2D} = 1/(\mu R_S e)$ (e is the electron charge). As shown in Figure 3(c), $n_{2D} \sim 3 \cdot 10^{13} cm^{-2}$ (green diamonds), a typical value for LAO/STO interfaces. The analysis of the Hall data measured directly across the bridge and in the large areas yields comparable carrier densities, as can be observed in the same Figure. We observe that the values shown in Figure 3 change by a factor of 3 for channel widths spanning almost two orders of magnitude from 500 nm to $10\mu m$,²⁹ as well as for the large areas of different devices. Fluctuations of this amplitude in the sheet resistance and mobility are fully compatible with variations observed from sample to sample, as reported in the literature by different groups for the same growth conditions. These results allow us to affirm that processing and confinement down to the sub-micron scale do not alter the carrier population and the transport properties, which appear to be homogeneous in the different areas of the sample.

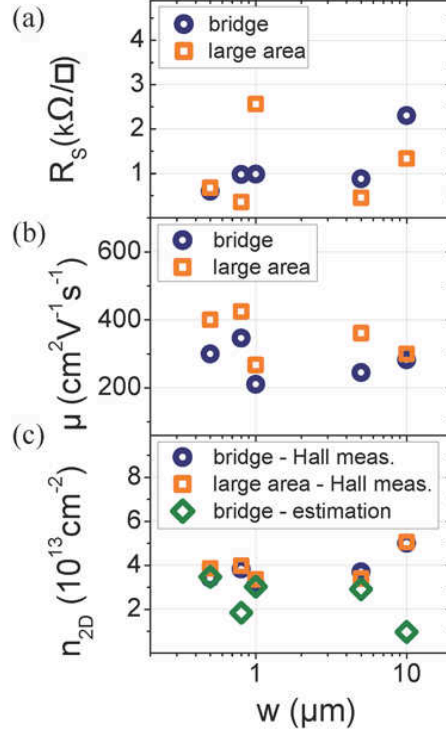


FIG. 3. (Color online) Transport parameters measured at 1.5 K of bridges of different width (blue circles) and of the adjoining large areas (orange squares): sheet resistance (a), mobility (b) and number of carriers (c). The green diamonds in panel (c) are the number of carriers estimated using the formula $n_{2D} = 1/(\mu R_S e)$ with μ and R_S from panels (a) and (b).

When cooled to millikelvin temperatures, these devices exhibit superconducting behavior. We measured voltage vs. current ($V-I$) characteristics at $T=40$ mK in a dilution refrigerator equipped with copper powder filters, using a four terminal configuration. Figure 4(a) and (b) show $V-I$ plots of the 500 nm and 800 nm wide devices revealing a superconducting state for these LAO/STO structures in the sub-micron range. The critical current densities are 150 and 430 $\mu\text{A}/\text{cm}$ for the 500 nm, 800 nm bridges respectively. These values are in line with a previous work⁴ where large-scale devices were measured. Their scatter is of the same order of that observed in transport parameters in the normal state (see Figure 3). The critical current can be tuned applying a gate voltage. Figure 4 shows the modulation of the $V-I$ characteristics for the 500 nm and 800 nm devices obtained in a back-gate configuration.⁵ We observe that a complete suppression of the critical current occurs for $V_g=-100$ V for the 500 nm device (panel (a)). For the 800 nm device, the zero resistance state is lost only below $V_g=-160$ V (panel b).

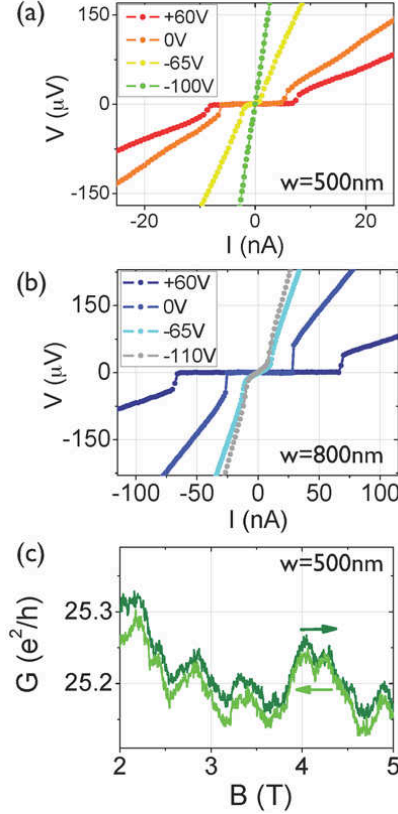


FIG. 4. (Color online) Low temperature characterization of the mesoscopic bridges. Panels (a) and (b) show the gate modulation of the $V - I$ characteristics for the 500 nm and 800 nm wide devices respectively. Panel (c) shows magnetoconductance fluctuations measured for the 500 nm bridge. The conduction state was set using field effect. The two traces refer to opposite directions of the field sweep. All the measurements presented in this figure were carried out at 40 mK.

In the normal state, the confinement of the 2DEG allows us to access the mesoscopic transport regime which, for phase coherent transport, manifests itself with the appearance of universal conductance fluctuations.^{30,31} UCF stem from quantum interference of phase-coherent electron waves scattered by impurities in a sample with dimensions L comparable to the phase coherence length l_φ . For $L = l_\varphi$ the amplitude of such fluctuations is expected to have the universal value e^2/h . Estimations of l_φ in LAO/STO interfaces yield values in the range of 100-200 nm at 1.5 K.^{7,20,32} Therefore our small bridges are expected to display UCF at low temperatures, albeit with a reduced amplitude since their dimensions are still larger than l_φ .

Figure 4(c) shows a magnetoconductance trace of the 500 nm wide device measured at

40 mK. The aperiodic fluctuations which can be seen have all the fingerprints of UCF. The two traces shown in the plot refer to the two sweep directions of the magnetic field, demonstrating the reproducibility of the fluctuation pattern. The phase-coherence length l_φ can be calculated from the typical average magnetic field spacing of the fluctuations ΔB_c via the equation:^{30,31} $\Delta B_c = C\Phi_0/(l_\varphi^2)$, where Φ_0 is the quantum of flux and C is a constant of the order of unity.³³ This estimation leads to $l_\varphi \approx 110 \pm 20$ nm. If we now consider the amplitude of the fluctuations, we observe that it is reduced with respect to the universal value. For the curve shown in Figure 4(c) it amounts to about 8% of e^2/h . A reduction in the amplitude is indeed expected when the mesoscopic channel has dimensions larger than l_φ . In this case, the channel may be subdivided into coherent areas of dimensions $l_\varphi \times l_\varphi$; the conductance fluctuations of each of these areas will be of order e^2/h and all the areas in the channel will add incoherently, leading to classical self-averaging. The resulting conductance fluctuations will be reduced by a factor proportional to $\sqrt{wl/l_\varphi^2}$, with w and l the width and length of the bridge respectively.³⁰ Considering our geometry, our results are in good numerical agreement with this argument.

In summary, we reported a detailed study of nanodevices based on the 2DEG at the LAO/STO interface. Mesoscopic bridges with widths down to 500 nm were realized using electron beam lithography. Possible damage to the STO substrate, such as oxygen losses, were avoided by resorting to an amorphous STO template. The detailed transport characterization reveals that processing and confinement down to the sub-micron scale do not alter substantially the carrier profile and that the samples are homogeneous down to the scale of our smallest bridges. The confinement of the 2DEG in the in-plane direction results in universal conductance fluctuations that were observed in magnetotransport at low temperatures. The devices show superconducting behavior, with a critical current tunable using field effect. The observation of a zero-resistance state in LAO/STO nanodevices opens exciting perspectives for the study of quasi-one dimensional superconductivity and for the realization of devices such as tunable Josephson junctions.

We thank P.Zubko for careful reading of the manuscript and M. Lopes and S. C. Müller for their technical assistance. This work was supported by the Swiss National Science Foundation through the National Center of Competence in Research, Materials with Novel Electronic Properties, MaNEP, division II, and the European Union through the project OxIDes.

REFERENCES

- ¹A. Ohtomo and H. Y. Hwang, *Nature (London)* **427**, 423 (2004).
- ²J. Mannhart and D. G. Schlom, *Science* **327**, 1607 (2010).
- ³P. Zubko, S. Gariglio, M. Gabay, P. Ghosez, and J.-M. Triscone, *Ann. Rev. Cond. Matter Phys.* **2**, 141 (2011).
- ⁴N. Reyren, S. Thiel, A. D. Caviglia, L. Fitting Kourkoutis, G. Hammerl, C. Richter, C. W. Schneider, T. Kopp, A.-S. Ruetschi, D. Jaccard, M. Gabay, D. A. Muller, J.-M. Triscone, and J. Mannhart, *Science* **317**, 1196 (2007).
- ⁵A. D. Caviglia, S. Gariglio, N. Reyren, D. Jaccard, T. Schneider, M. Gabay, S. Thiel, G. Hammerl, J. Mannhart, and J.-M. Triscone, *Nature* **456**, 624 (2008).
- ⁶C. Bell, S. Harashima, Y. Kozuka, M. Kim, B. G. Kim, Y. Hikita, and H. Y. Hwang, *Phys. Rev. Lett.* **103**, 226802 (2009).
- ⁷A. D. Caviglia, M. Gabay, S. Gariglio, N. Reyren, C. Cancellieri, and J. M. Triscone, *Phys. Rev. Lett.* **104**, 126803 (2010).
- ⁸M. Ben Shalom, M. Sachs, D. Rakhmievitch, A. Palevski, and Y. Dagan, *Phys. Rev. Lett.* **104**, 126802 (2010).
- ⁹M. Basletic, J. Maurice, C. Carrétéro, G. Herranz, O. Copie, M. Bibes, E. Jacquet, K. Bouzehouane, S. Fusil, and A. Barthélémy, *Nature Mater.* **7**, 621 (2008).
- ¹⁰N. Reyren, S. Gariglio, A. D. Caviglia, D. Jaccard, T. Schneider, and J.-M. Triscone, *Appl. Phys. Lett.* **94**, 112506 (2009).
- ¹¹A. D. Caviglia, S. Gariglio, C. Cancellieri, B. Sacépé, A. Fête, N. Reyren, M. Gabay, A. F. Morpurgo, and J. M. Triscone, *Phys. Rev. Lett.* **105**, 236802 (2010).
- ¹²M. Ben Shalom, A. Ron, A. Palevski, and Y. Dagan, *Phys. Rev. Lett.* **105**, 206401 (2010)
- ¹³S. Gariglio, M. Gabay, and J.-M. Triscone, *Nature Nano.* **5**, 13 (2010).
- ¹⁴R. P. Kaur, D. F. Agterberg, and M. Sigrist, *Phys. Rev. Lett.* **94**, 137002 (2005).
- ¹⁵B. Liu and X. Hu, *Phys. Rev. B* **81**, 144504 (2010).
- ¹⁶C. Cen, S. Thiel, G. Hammerl, C. W. Schneider, K. E. Andersen, C. S. Hellberg, J. Mannhart, and J. Levy, *Nat. Mat.* **7**, 298 (2008).
- ¹⁷C. Cen, S. Thiel, J. Mannhart, and J. Levy, *Science* **323**, 1026 (2009).

- ¹⁸Y. Xie, C. Bell, T. Yajima, Y. Hikita, and H. Y. Hwang, *Nano Lett.* **10**, 2588 (2010).
- ¹⁹C. W. Schneider, S. Thiel, G. Hammerl, C. Richter, and J. Mannhart, *Appl. Phys. Lett.* **89**, 12210 (2006).
- ²⁰D. Rakhmilevitch, M. Ben Shalom, M. Eshkol, A. Tsukernik, A. Palevski, and Y. Dagan, *Phys. Rev. B* **82**, 235119 (2010).
- ²¹V.E. Henrich, G. Dresselhaus, and H.J. Zeiger, *Phys. Rev. B* **17**, 4908 (1978).
- ²²We used two layers of PMMA, with 495 K and 950 K molecular weight, both with a 3% solid content in anisole, for a total thickness of ~ 300 nm. The double layer was used in order to facilitate the subsequent lift-off step.
- ²³C. B. Samantaray and J. T. Hastings, *J. Vac. Sci. Technol. B* **26**, 2300 (2008)
- ²⁴A similar template approach has been reported recently by N. Banerjee, M. Huijben, G. Koster, and G. Rijnders, *Appl. Phys. Lett.* **100**, 041601 (2012).
- ²⁵C. Cancellieri, N. Reyren, S. Gariglio, A. D. Caviglia, A. Fête, and J.-M. Triscone, *Europhys. Lett.* **91**, 17004 (2010).
- ²⁶At the end of our fabrication process, the interface between the STO substrate and the amorphous STO layer is observed to be insulating.
- ²⁷G. Pearson and H. Suhl, *Phys. Rev.* **83**, 768 (1951).
- ²⁸F. Kuchar and P. Frankus, *Phys. Rev. B* **16**, 874 (1977).
- ²⁹The lateral dimension of each bridge is confirmed using AFM topography.
- ³⁰P. A. Lee, A. Stone, and H. Fukuyama, *Phys. Rev. B* **35**, 1039 (1987).
- ³¹C. W. J. Beenakker and H. van Houten, *Solid State Physics* **44**, 1 (1991).
- ³²D. A. Dikin, M. Mehta, C. W. Bark, C. M. Folkman, C. B. Eom, and V. Chandrasekhar, *Phys. Rev. Lett.* **107**, 056802 (2011).
- ³³An exact estimation of the correlation field ΔB_c is given by the full width at half maximum of the magneto conductance autocorrelation function, which fully captures the characteristic length scales of a mesoscopic system.